Hindawi
Shock and Vibration
Volume 2024, Article ID 3686948, 15 pages
https://doi.org/10.1155/2024/3686948

Research Article

Study on the Influence of Missile Cabin on Fragment Velocity under Explosive Detonation Impact

Xin Li,[1,2] **Weili Wang**,[1] **Zhengfeng Liang**,[2] **Jun Dong**,[3] **and Jiaojiao Tang**[2]

[1]*College of Weaponry Engineering, Naval University of Engineering, Wuhan 430033, China*
[2]*Xi'an Modern Chemistry Research Institute, Xi'an 710065, China*
[3]*School of Aerospace Engineering, Xi'an Jiaotong University, Xi'an 710049, China*

Correspondence should be addressed to Xin Li; syhshanxi2008@126.com and Jun Dong; welcome204dj@163.com

Received 2 November 2023; Revised 23 December 2023; Accepted 30 December 2023; Published 18 January 2024

Academic Editor: Xiuquan Liu

For the air-to-air missile warhead, there is a cabin with a certain thickness at a distance around the fragments. At present, the influence of missile cabin has not yet been taken into account in the study of fragment velocity. In this paper, based on the law of conservation of energy, the theoretical equation of fragment velocity considering the kinetic energy of cabin debris was deduced. Then, the rationality of the theoretical formula is validated through the static explosion experiments of two prototype warheads, one with a titanium alloy cabin and the other without any cabin. It was found that after the warhead is equipped with the cabin, part of the energy is consumed to drive the cabin debris, resulting in a decrease in fragment velocity, but the velocity of cabin debris was greater than that of fragment of warheads without any cabin. Besides, through numerical simulation, the driving process of fragments and cabin debris during explosive detonation loading of the warhead with the cabin was studied, which can be divided into six stages, and the error between numerical result and experimental value is not more than 4.8%. Finally, the variety regulation of fragment velocity and cabin debris velocity at different interval distances was further studied by numerical simulation. The results indicate that fragment velocity of warheads with cabin at different interval distances is basically the same, but cabin debris velocity decreases with the increase of interval distance. This conclusion can provide a reference for the structural design and fragment velocity evaluation of warheads with cabin.

1. Introduction

The fragmentation-kill warhead is the most commonly used warhead type in current air defense and antimissile missile systems. As an important part of the missile to damage the target or complete the established combat mission, the generated high-velocity fragment group is used to achieve high-speed impact, ignition, and detonation to damage the air target. The fragment velocity is an important indicator to measure the power performance of the fragmentation-kill warhead. Accurate measurement of the fragment velocity is the basis of the warhead power evaluation. Therefore, it is of great significance to study the fragment velocity of the warhead.

Researchers at home and abroad have carried out a lot of research on the fragment velocity of fragmentation-kill warheads. The most typical one is the typical equation based on energy distribution proposed by Gurney [1]. In the derivation process, it was assumed that all parts of the cylindrical shell were broken under the same stress, and the generated fragments had the same initial velocity along the axis of the cylindrical shell, which is suitable for calculating the initial fragment velocity of the cylindrical shell. Subsequently, based on the Gurney formula, the velocity of semi-prefabricated and fully prefabricated fragments of the fragmentation-kill warhead was studied [2–6]. For prefabricated fragment warheads, considering the energy loss caused by the escape of explosive gas through the gaps between prefabricated fragments laid on thin shells, a coefficient is usually added to the equation, with a general value of 0.9. Some people have also studied the velocity distribution of multilayer fragments of the fragmentation-kill warhead. The results showed that the outer fragment

velocity was greater than the inner fragment velocity [7–12]. When using eccentric directional detonation, due to the different impulses applied to the radial fragments, there are differences in the energy allocated to the radial fragments by the explosive, resulting in a gradient distribution of radial fragment velocity [13, 14]. Among them, the radial velocity of single-point eccentric detonation can be obtained by adding a correction variable function, introducing an energy distribution point, and deriving the theory of detonation impulse effect. The radial velocity of two-point eccentric detonation is mainly obtained based on the Mach wave theory of detonation collision. From the above research, it can be seen that the fragment velocity is carried out specifically for fragments in contact with explosives [15].

For the air-to-air missile warhead, fragmentation-kill warhead is generally built inside the missile cabin by mechanical connection. As the missile body structure system, the cabin is to make the missile have a good aerodynamic shape and withstand various loads during the flying and launch of missiles. It is often made of TC4 titanium alloy, and the wall thickness is within the range of 1 mm to 4 mm [16–18]. In the process of missile action, the explosive detonation inside the fragmentation-kill warhead forms high-temperature and high-pressure products. In addition to driving the fragments, it is also necessary to drive the missile cabin. Therefore, fragment velocity will inevitably be affected after adding the cabin. However, so far, there has been no research on the fragment velocity under the influence of missile cabins.

In this paper, therefore, the fragment velocity of warhead with cabin is the main object of analysis, and theoretical analysis, experimental verification, and numerical simulation are used as the analysis method [19–22], with the ultimate goal of clarifying the influence of missile cabin on fragment velocity under explosive detonation impact. It has important practical guidance significance for practitioners in the design and lethality assessment of air-to-air missile warheads. Of course, it can also serve as the basis for studying the dynamic response characteristics of double-layer shell under detonation driving.

In Section 2, the theoretical equation of fragment velocity considering the kinetic energy of cabin debris is derived according to the law of conservation of energy. In Section 3, the fragment velocity and cabin debris velocity of noncabin/cabin-containing warheads are studied by static explosion experiments on the ground. In Section 4, the driving process of fragments and cabin debris during explosive detonation loading of the warhead with cabin is analysed by numerical simulation, and the rationality of the numerical simulation method is verified by comparing it with the experimental results. In Section 5, the relationship between ratios of interval distances to the charge radius (l/r) and fragment velocity and cabin debris velocity is then further analysed. Conclusions are drawn in Section 6.

2. Theoretical Analysis

When the length-diameter ratio of the warhead exceeds 2, it is generally believed that the fragment velocity and the cabin debris velocity near the equatorial plane are not affected by the rarefaction wave. At this time, it can be simplified into a two-dimensional model problem for research. Figure 1 shows the schematic diagram of the cabin-containing warhead structure with explosive at the center. It is mainly composed of the cabin, the fragments, and the main explosive. I is the detonation point, t is the wall thickness of the cabin, l is the interval distance between the cabin and the fragments (hereafter referred to as the interval distance), h is the fragment thickness, r is the charge radius, and l/r is the ratio of the interval distance to the charge radius.

After the explosive inside the warhead explodes, the generated high-temperature and high-pressure products diffuse around and act on the inner wall of the fragment. Under the action of radial pressure, the fragments are driven to accelerate, and then, it acts on the missile cabin to make it expand, break, and accelerate. According to the law of conservation of energy [23], the theoretical equation of the initial velocity of the fragment of the warhead containing the cabin can be derived. Before the derivation, the following assumptions were made:

(1) Fragments, cabin debris, and detonation products only flew along the radial direction, regardless of the movement along the axial direction of the charge

(2) The energy consumed in the process of cabin deformation and crushing was ignored

(3) The initial velocity of each fragment was equal

(4) Explosive exploded instantaneously, and detonation product velocity showed a radial linear distribution and is the same as the fragment velocity of the contacted fragment

(5) The initial velocity of each cabin debris was also equal

Then, the following equation can be made:

$$E_t = E_{f,k} + E_{c,k} + E_{p,k} + E_{p,e} + E_{a,e}, \tag{1}$$

where E_t is the gross energy of explosive detonation, $E_{f,k}$ is the kinetic energy of fragments, $E_{c,k}$ is the kinetic energy of detonation products, $E_{p,k}$ is the kinetic energy of cabin debris, $E_{p,e}$ is the internal energy of detonation products, and $E_{a,e}$ is the energy of an air shock wave.

The energy of each part was calculated separately below. The gross energy of explosive detonation is as follows:

$$E_t = m_e Q_v, \tag{2}$$

where m_e is the mass of explosive charge and Q_v is the explosive detonation heat.

The kinetic energy of fragments is calculated as follows:

$$E_{f,k} = \frac{1}{2} N_f m_f v_f^2, \tag{3}$$

where N_f is the quantity of fragments, m_f is the mass of a single fragment, and v_f is the initial velocity of fragments.

The wall thickness of the cabin was relatively thinner than the diameter of the warhead, so the kinetic energy of the cabin debris is approximately expressed as follows:

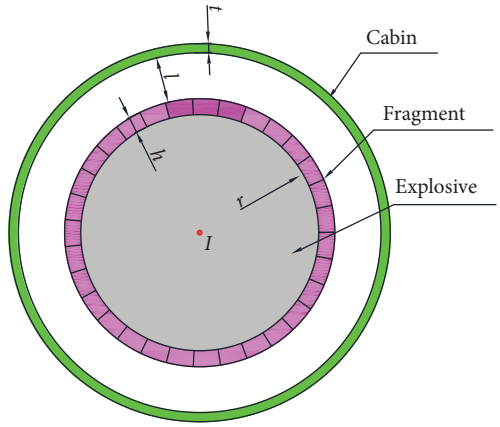

Figure 1: Structural diagram of the fragmentation-kill warhead with a cabin.

$$E_{c,k} = \frac{1}{2}\pi(r + h + l)tL\rho_c v_c^2, \tag{4}$$

where L is the length of the warhead, ρ_c is the density of the cabin, and v_c is the initial velocity of cabin debris.

The kinetic energy of the detonation products is as follows:

$$E_{p,k} = \frac{1}{4}m_e v_f^2. \tag{5}$$

The internal energy of detonation products is equal to the multiplication value of its mass and specific internal energy, that is,

$$E_{p,e} = \frac{m_e p}{\rho(\gamma - 1)}, \tag{6}$$

where p, ρ, and γ are, respectively, the pressure, density, and polytropic index of the detonation product when the fragment reaches the maximum velocity. According to the state equation of detonation products, it can be obtained:

$$\frac{p}{p_0} = \left(\frac{\rho}{\rho_0}\right)^{\gamma} = \left(\frac{\pi r^2 l}{\pi R^2 l}\right)^{\gamma} = \left(\frac{r}{R}\right)^{2\gamma}, \tag{7}$$

where R is the radius of the fragment to reach the maximum velocity and p_0 and ρ_0 are, respectively, the pressure and the density of the detonation product at the initial moment of the warhead detonation. According to the instantaneous detonation of the explosive, the pressure is assumed as follows:

$$p_0 = \frac{Q_V}{\rho_0(\gamma - 1)}. \tag{8}$$

Then, when $\gamma = 3$,

$$E_{p,e} = m_e Q_V \left(\frac{r}{R}\right)^4. \tag{9}$$

Assuming that the particle velocity behind the air shock wave front which is formed before the fragment is equal to the fragment velocity, the energy of the air shock wave can be expressed as follows:

$$E_{a,e} = m_a\left(\frac{1}{2}v_f^2 + \frac{p_a}{(k-1)\rho_a}\right), \tag{10}$$

where m_a is the mass of compressed air, p_a is the air shock wave pressure, and ρ_a is the compressed air density.

According to the basic equation of shock wave, it can be obtained that

$$v_f^2 = (p_a - p_{a0})\left(\frac{1}{\rho_{a0}} - \frac{1}{\rho_a}\right), \tag{11}$$

where ρ_{a0} is the air density and p_{a0} is the initial pressure of air. Considering that the air particle velocity after the shock wave front reaches several kilometers per second, and the wavefront pressure reaches 5~10 MPa, which belongs to the strong air shock wave, the strong shock wave equation is adopted:

$$\frac{\rho_a}{\rho_{a0}} = \frac{k+1}{k-1}. \tag{12}$$

When p_{a0} is ignored, it can be obtained that

$$v_f^2 = \frac{p_a}{(k-1)\rho_a}. \tag{13}$$

According to the law of conservation of mass, it can be concluded that

$$m_a = \pi L\left(r_a^2 - r^2\right)\rho_{a0} = \pi L\left(r_a^2 - R^2\right)\rho_a, \tag{14}$$

where r_a is the radius of the shock wave front.

It is assumed that the air in the air shock wave dissociates, then $k \approx 1.25$. So $(\rho_a/\rho_{a0}) = (k+1)/(k-1) = 9$. Also, it is obtained that

$$m_a = \frac{9}{8}\pi l\left(R^2 - r^2\right)\rho_{a0}, \tag{15}$$

$$E_{a,e} = \frac{27}{16}\pi l\rho_{a0}\left(R^2 - r^2\right)v_f^2. \tag{16}$$

Substituting the above equations (2), (3), (5), (9), and (16) into equation (1), the fragment velocity can be calculated as follows:

$$v_f = \sqrt{\frac{m_e Q_V - \pi(r + h + l)tL\rho_c v_c^2 - m_e Q_V (r/R)^4}{(1/2)N_f m_f + (1/4)m_e + (27/16)\pi L\rho_{a0}\left(R^2 - r^2\right)}}. \tag{17}$$

It can be seen from equation (17) that the fragment velocity of the warhead with the cabin is related to the interval distance, the cabin debris velocity, and the radius of the moment when the fragment reaches the maximum flying velocity. With the increase of the interval distance, the mass of the cabin is bound to increase when the wall thickness of the cabin is constant. Because the change trend of the cabin debris velocity cannot be judged, the energy used to drive the cabin debris cannot be quantified. Also, it is clear that the detonation energy of the explosive will be used to drive the cabin debris. At the same time, according to equation (7), for the noncabin warhead, when the pressure of the detonation product is reduced to the

moment when the fragment reaches the maximum velocity, the expansion radius is about 2 times the initial radius [24]. For the warhead containing the cabin, considering the yield strength of the cabin, the pressure of the detonation product at the moment when the fragment reaches the maximum velocity is relatively large, and the expansion radius is lower than that of the noncabin warhead, that is, the distance of the fragment is close at the same time. Based on the above analysis, it can be seen that the fragment velocity of the cabin-containing warhead decreases compared with that without cabin.

3. Experiments Verification

3.1. Prototype Design. In order to verify the rationality of the theoretical analysis, two warhead prototypes were prepared, one without any cabin and one with the cabin, as shown in Figure 2. For the noncabin prototype, the weight was about 9.0 kg, the diameter of the charge was 100 mm, and the length was 200 mm. The central detonation mode was adopted. It was considered that the fragment velocity near the equatorial plane was not affected by the rarefaction wave [5, 25, 26]. The prototype was filled with fully prefabricated tungsten alloy fragments. There were 20 ring layers with 31 fragments in each layer (620 fragments in total). The mass of a single fragment was 8.75 g. The explosive charge was an HMX-based PBX high-energy explosive with a mass of 2.89 kg and a loading ratio of 0.533. According to equation (18), the initial velocity of the fragment of the noncabin prototype was 1, 622.7 m/s. Except for the cabin, the structure of the prototype with the cabin was exactly the same as that of the prototype without the cabin. The cabin was made of TC4 titanium alloy with a wall thickness of 3 mm, an interval distance of 10 mm, and a cabin mass of 1.12. Considering the mass of the cabin, the loading ratio was 0.441. The initial velocity of the fragment of the prototype with the cabin was calculated to be 1, 503.9 m/s by using the following equation:

$$v_0 = 0.9 \cdot \sqrt{2E}\sqrt{\frac{\beta}{1 + 0.5\beta}}. \tag{18}$$

3.2. Test Layout. The test layout is shown in Figure 3. Off target was arranged at 1 m, 2 m, 3 m, 4 m, and 5 m away from the explosion center, and a 180° arc target plate was arranged at 6 m away from the explosion center on the other side. The height of the target plate was 4 m, and the thickness of the target plate was 6 mm. A high-speed camera was set up at about 100 m away from the back of the target plate to observe the flame generated by the fragments and cabin debris penetrating through the target plate. Because the titanium alloy is a flammable metal, the cabin debris deformed at high speed to produce adiabatic shear bands when penetrating through the steel plate, and the elements such as Ti and Al on the surface experienced violent oxidization exothermic reaction at high temperature to form a self-sustaining high-temperature flame combustion layer [27, 28]. The generated flame light showed a scattered firework, while the flame light generated by the tungsten alloy fragment penetrating through the steel plate was small, and only a single bright light appeared. Therefore, the tungsten alloy fragment and the cabin debris could be distinguished by the shape and intensity of the bright light generated by the impact on the steel plate, and the fragment velocity and the cabin debris velocity could be obtained according to the attenuation coefficient measured by the off target.

3.3. Data Processing Method. The time of fragments and cabin debris reaching different distances can be measured by five off targets. According to GJB5232.3-2004 Test Method for Arena of Tactical Missile Warhead Performance-Part 3: Determination of Fragment Initial Velocity in Fixed Point Explosion Test, the velocity attenuation coefficient, α, of fragments and cabin debris can be calculated as shown in the following equation:

$$\alpha = \frac{\sum_{i=1}^{n} S_i \cdot \sum_{i=1}^{n} \ln V_i - n\sum_{i=1}^{n} S_i \ln V_i}{n\sum_{i=1}^{n} S_i^2 - \left(\sum_{i=1}^{n} S_i\right)^2}, \tag{19}$$

where i is the off target number, R_i is the distance (m) from the detonation center to i^{th} off target, and S_i is the distance (m) from the detonation center to the midpoint of two adjacent off targets, and it can be calculated as follows:

$$S_i = R_{i-1} + \frac{R_i - R_{i-1}}{2}. \tag{20}$$

T_i is the flying time (ms) of the fragment or cabin debris from the detonation center to the i^{th} off target and Vi is the average flying velocity (m/s) of fragments or cabin debris between two adjacent off targets, and it can be expressed as follows:

$$V_i = \frac{R_i - R_{i-1}}{T_i - T_{i-1}}. \tag{21}$$

Utilizing the obtained velocity attenuation coefficient, the initial fragment velocity was derived according to the formula (22), where v_x is the instantaneous velocity of fragments at 3 m, which is approximately equal to the average velocity of fragments within 6 m.

$$v_0 = \frac{v_x}{e^{-\alpha \cdot x}}. \tag{22}$$

3.4. Experimental Results and Discussion

3.4.1. High-Speed Photograph. The typical photos of the static explosion on the ground using high-speed photography for noncabin prototype and cabin-containing prototype are shown in Figures 4 and 5.

By comparing Figures 4 and 5, it can be seen that when the noncabin prototype was detonated in the center, the tungsten alloy fragment near the equatorial plane penetrated through the steel plate at 3.8 ms to generate flame light, and then the flame light spread to both sides. Finally, the tungsten alloy fragment at both ends penetrated through the steel plate to generate flame light. At the same time, it can be observed that the firelight formed by the tungsten alloy fragment hitting the steel plate was dotted, and the firelight area formed by a single fragment was small. When the center

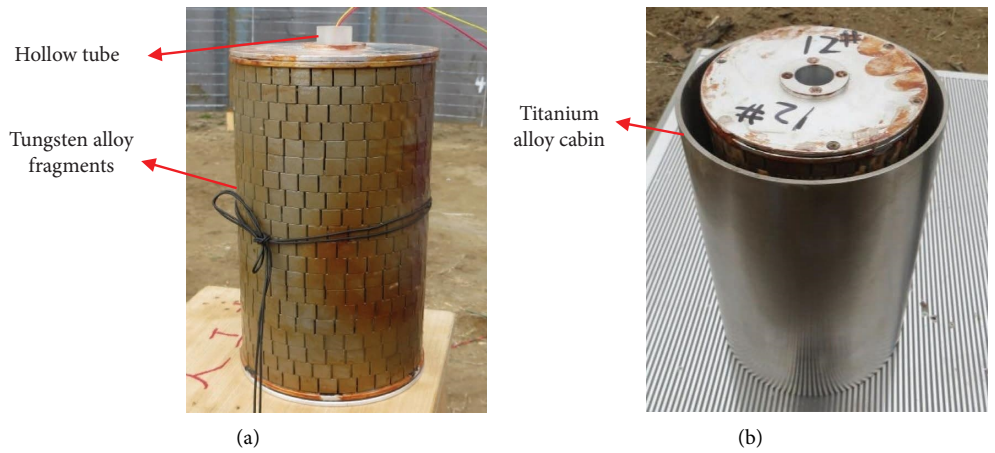

Figure 2: Prototypes in the experiments. (a) Noncabin prototype. (b) Cabin-containing prototype.

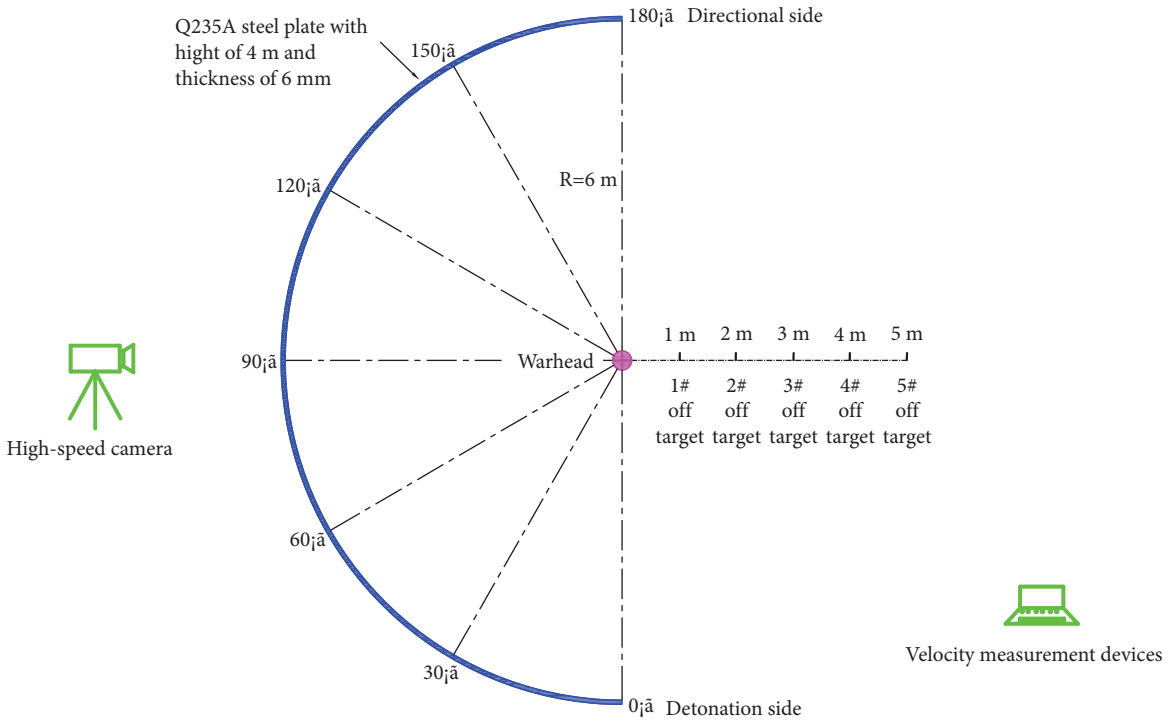

Figure 3: Test layout.

of the cabin-containing prototype was detonated, at the moment of explosive detonation loading at 3.2 ms, the titanium alloy cabin debris penetrated through the steel plate to produce a flame light, and the formed firelight showed a scattered firework, and the flame light area was large. At 3.6 ms, the titanium alloy cabin debris group penetrated through the steel plate, and at 5.0 ms, the tungsten alloy fragments near the equatorial plane passed through the steel plate, which is obviously lagging behind the fame light generated by the cabin debris. It indicated that the cabin debris velocity was greater than that of tungsten alloy fragments, which is consistent with the conclusion that the outer layer fragment velocity is greater than the inner layer fragment velocity [7–9], and the velocity of tungsten alloy fragments was also reduced after adding the cabin. This is because the time required for tungsten alloy fragments to produce flame light at the same position was increased, compared with the noncabin prototype. Similarly, the time required for tungsten alloy fragments at both ends to penetrate through the target plate to generate flame light was greater than that of tungsten alloy fragments at both ends of the noncabin prototype. The duration of the flame light formed by the fragments of the titanium alloy cabin penetrating through the steel plate was significantly longer than that of the tungsten alloy fragment. At 5.0 ms, the bright light generated by the tungsten alloy fragment penetrating through the steel plate was still strong. At the time of 16.6 ms, the brightness of the firelight gradually darkened.

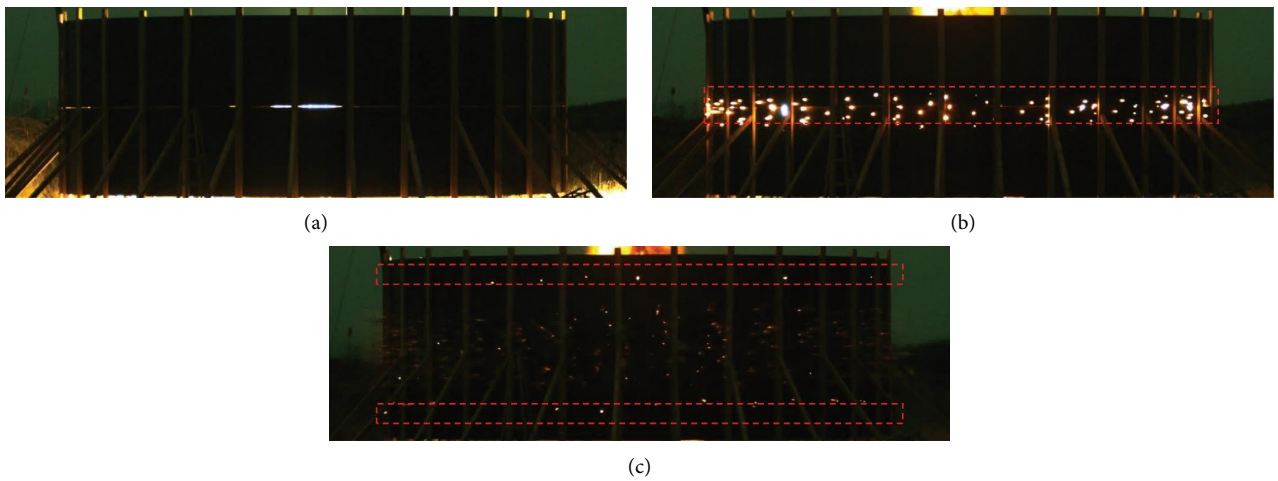

(a) (b) (c)

Figure 4: Typical photos for noncabin prototype during static explosion by using high-speed photography. (a) $t = 0$ ms. (b) $t = 3.8$ ms. (c) $t = 5.2$ ms.

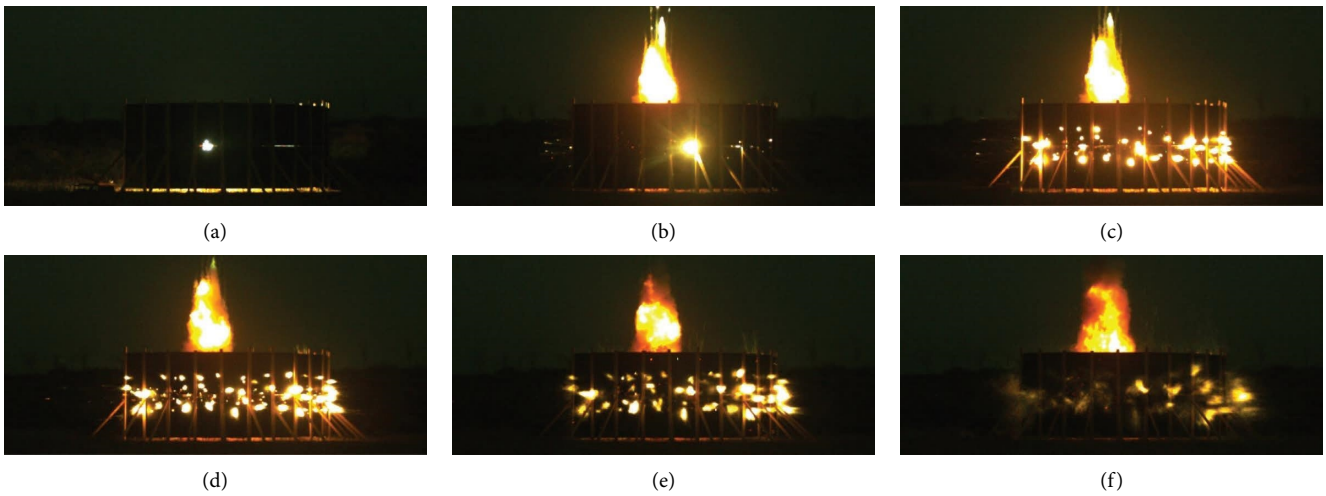

(a) (b) (c) (d) (e) (f)

Figure 5: Typical photos for cabin-containing prototype during static explosion by using high-speed photography. (a) $t = 0$ ms. (b) $t = 3.2$ ms. (c) $t = 3.6$ ms. (d) $t = 5.0$ ms. (e) $t = 7.0$ ms. (f) $t = 16.6$ ms.

3.4.2. Fragment Velocity and Cabin Debris Velocity. Accordingly, the attenuation coefficient of fragments was calculated to be 0.022, and the attenuation coefficient of cabin debris was 0.032. The fragment velocity and cabin debris velocity calculated according to the attenuation coefficient are shown in Table 1.

It can be seen from Table 1 that the initial velocity of the fragment near the equatorial plane of the noncabin prototype was 1,686.7 m/s, which is basically consistent with the theoretical calculation value of 1,622.7 m/s by the modified Gurney formula. The initial velocity of the fragment near the equatorial plane of the cabin-containing prototype was 1,281.9 m/s, which is significantly lower than the theoretical value of 1, 503.9 calculated by the modified Gurney formula. It indicates that the modified Gurney formula is no longer suitable for calculating the fragment velocity of the cabin-containing warhead. The initial cabin debris velocity near the equatorial plane was 1,834.6 m/s. From the perspective of energy conservation, part of the energy of the explosive detonation product was used for the acceleration of the cabin, so that the energy used to drive the fragment was relatively reduced. Therefore, the initial velocity of the fragment will decrease after adding the cabin, which is consistent with the theoretical analysis results.

4. Numerical Simulation

4.1. Calculation Model and Parameters. In order to study the influence of the cabin on the acceleration process of fragments under explosive detonation loading, LS-DYNA dynamic simulation software was used for numerical simulation. The calculation model was composed of titanium alloy cabin, explosive, and tungsten alloy fragments, as shown in Figure 6(a). The thickness of the cabin wall was 3 mm, and the charge diameter was Φ100 mm. The fragment thickness was 5 mm, and there were 31 pieces in total. The

Table 1: Results of fragment velocity and cabin debris velocity.

Prototype	Fragments near the equatorial plane			Fragments at both ends			Cabin debris near equatorial plane		
	Time (ms)	Average velocity within 6 m (m/s)	Initial velocity (m/s)	Time (ms)	Average velocity within 6 m (m/s)	Initial velocity (m/s)	Time (ms)	Average velocity within 6 m (m/s)	Initial velocity (m/s)
Noncabin	3.8	1578.9	1686.7	5.2	1153.8	1232.5	—	—	—
With cabin	5.0	1200.0	1281.9	7.0	857.1	915.6	3.6	1666.7	1834.6

interval distance was 10 mm, and the ratio of the interval distance to the charge radius was 0.2. At the same time, for the convenience of comparison, the detonation process of the noncabin warhead was numerically simulated, and the calculation model is shown in Figure 6(b). The titanium alloy cabin and fragment were modeled by a single-point integral Lagrange hexahedron grid. The element used the Lagrange algorithm. The explosive was modeled by the Euler hexahedron grid. The element used the single-point Euler algorithm. The single-layer grid multimaterial fluid-solid coupling MMALE algorithm was used for coupling calculation. The grid size was 0.5 mm, and the cm-g-μs unit system was used for modeling.

The explosive was HMX-based PBX explosive, and the components mainly included 62% HMX, 18% Al, 9% binder, and 11% other content. The JWL state formula and the MAT _ HIGH _ EXPLOSIVE _ BURN detonation model were used to describe it. The JWL state equation was a state equation determined by the experimental method, which can accurately describe the pressure, energy, and volume expansion characteristics of the detonation product during the detonation driving process. It is expressed as follows:

$$p = A\left(1 - \frac{\omega}{R_1 V}\right)\exp\left(-R_1 V\right) + B\left(1 - \frac{\omega}{R_2 V}\right)\exp\left(-R_2 V\right) + \frac{\omega E}{V}, \tag{23}$$

where V is the relative specific volume of the detonation product, E is the initial internal energy of the explosive, and A, B, R_1, R_2, and ω are constants that characterize the detonation characteristics of the explosive, and the material parameters of the explosive are shown in Table 2 [29].

The fragment was 93W alloy, which is made by using a PLASTIC _ KINEMATIC kinematic hardening model. The parameters are shown in Table 3 [30], and the cabin was TC4 titanium alloy, and the parameters are shown in Table 4.

4.2. Detonation Driving Process. The detonation driving process of the noncabin warhead is shown in Figure 7. When $l/r = 0.2$, the detonation driving process of the warhead with cabin is shown in Figure 8.

It can be seen from Figure 7 that after the detonation of the noncabin warhead explosive, the detonation wave propagated in the explosive, and the reflection of the shock wave was formed after reaching the fragment. The detonation of the explosive completely formed a high-temperature and high-pressure detonation products. Under the action of the detonation wave and the detonation product, the fragments flew outward. It can be seen from Figure 8 that when the warhead contained a cabin and $l/r = 0.2$, the explosive detonation product first drove the fragment to fly outward. Then, they expanded and broke the cabin to form fragments and drove the fragment to fly outward. The specific detonation driving process can be divided into six stages: (I) fragment driving acceleration stage; (II) overflow stage of detonation products; (III) expansion and rupture stage of the cabin; (IV) collision and separation stage of fragments and cabin debris; (V) further acceleration stage of fragments and cabin debris; (VI) stable flying phase of fragments and cabin debris. They are shown in Figure 9. In the figure, t_1 is the moment when the detonation product begins to overflow, t_2 is the moment when the cabin begins to expand, t_3 is the moment when the cabin begins to burst, t_4 is the moment when the fragment collides with the cabin debris, t_5 is the moment when the cabin ruptures, t_6 is the moment when the fragment is separated from the cabin debris, t_7 is the moment when the fragment reaches the initial velocity, and t_8 is the moment when the cabin debris reaches the initial velocity.

4.2.1. Fragment Driving Acceleration Stage. After the detonation of the explosive, the detonation wave propagated in the explosive and formed a reflection of the shock wave after reaching the inner surface of the fragment. After about 5 μs, the detonation of the explosive completely formed high-temperature and high-pressure detonation gas products. Under the high pressure of the detonation wave and the detonation product, the fragment began to accelerate and disperse around.

4.2.2. Overflow Stage of Detonation Products. Because the fragment was a fully prefabricated structure, at the moment when the detonation drove the fragment to fly outward, gaps appeared between the fragments. At this time, the detonation product began to flow through the gap to overflow outward. And because the velocity of the detonation product was higher than that of the fragment, the detonation product diffused outward before the fragment and surrounded the fragment.

4.2.3. Expansion and Rupture Stage of the Cabin. When the detonation product diffused to the surface of the cabin, the cabin expanded and deformed rapidly under the condition of high pressure and high strain rate. When the pressure of the detonation product exceeded the dynamic yield strength of the cabin, cracks were formed, and then, debris was generated. When the ratio of interval distance to charge radius was 0.2, the cabin began to expand radially under the action of detonation products from 18.2 μs. At 20.4 μs, the cabin broke up, and the radius of the cabin expanded to 1.07 times of the initial radius.

4.2.4. Collision and Separation Stage of Fragments and Cabin Debris. When the cabin expanded and broke, due to the relatively low speed of the cabin debris and the relatively high speed of the fragments, the fragments and the cabin encountered and collided at a certain time to achieve energy transfer, and then, they were separated. When the ratio of the interval distance to the charge radius was 0.2, the collision time was 25 μs, and the separation time was 30 μs.

4.2.5. Further Acceleration Stage of Fragments and Cabin Debris. When the fragment was separated from the cabin debris because the velocity of the detonation product was

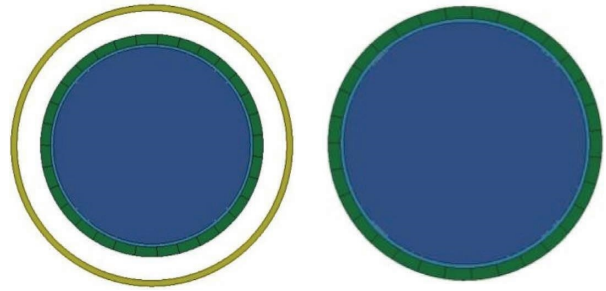

(a) (b)

Figure 6: Calculation model. (a) Cabin-containing warhead. (b) No-cabin warhead.

Table 2: Material parameters of HMX-based PBX explosive.

Density ($kg \cdot m^{-3}$)	Detonation pressure (GPa)	Detonation velocity ($m \cdot s^{-1}$)	A (GPa)	B (GPa)	R_1	R_2	ω
1818	31.86	8336	748.6	13.38	4.5	1.2	0.38

Table 3: Material parameters of 93W alloy.

Material	Density ($kg \cdot m^{-3}$)	Young's modulus (GPa)	Shear modulus (GPa)	Poisson's ratio	Yield stress (GPa)	Hardening coefficient
93W alloy	17600	357	7.9	0.303	2	1

Table 4: Material parameters of TC4 titanium alloy.

Material	Density ($kg \cdot m^{-3}$)	Young's modulus (GPa)	Shear modulus (GPa)	Tangent modulus (GPa)	Poisson's ratio	Yield stress (GPa)
TC4 titanium alloy	4419	96	41.9	1.125	0.36	1.098

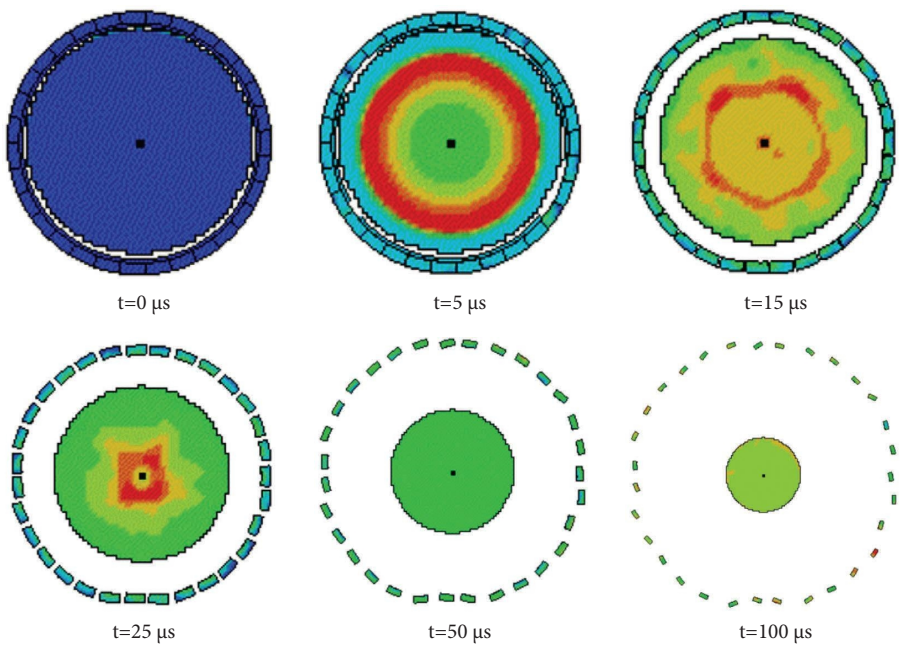

Figure 7: Detonation driving process of the noncabin warhead.

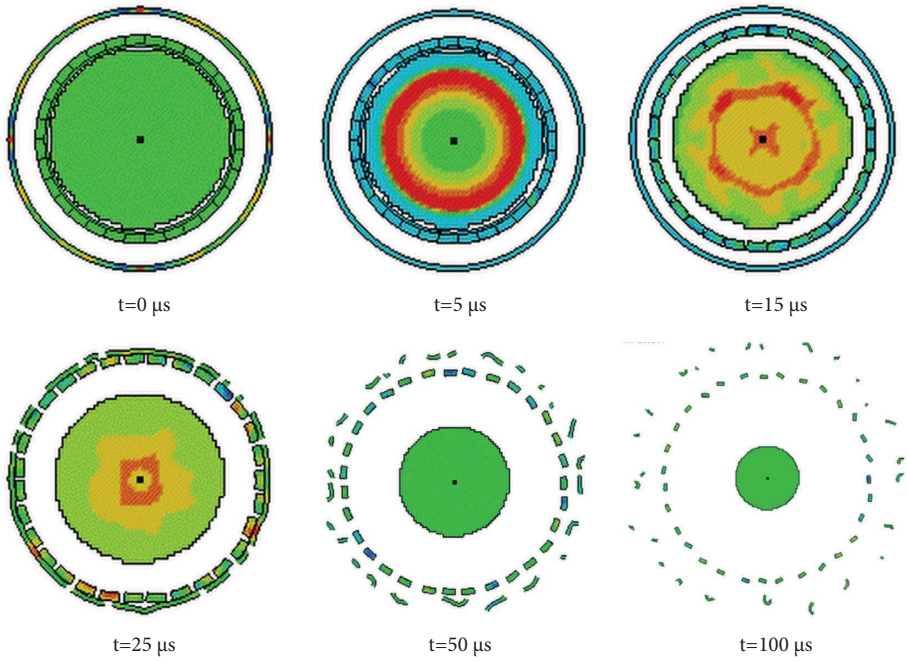

Figure 8: Detonation driving process of the warhead with cabin when $l/r = 0.2$.

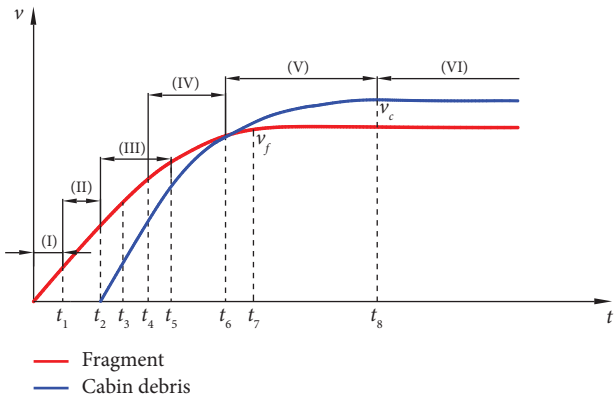

Figure 9: Acceleration process of fragments and cabin debris.

still greater than the fragment velocity and the cabin debris velocity, the fragment and the cabin debris were further accelerated. When the ratio of the interval distance to the charge radius was 0.2, the acceleration of the cabin debris was relatively faster, making the distance between the cabin debris and the fragment farther and farther.

4.2.6. Stable Flying Phase of Fragments and Cabin Debris. When the velocity of fragments and cabin debris were the same as that of detonation products, both of them reached the maximum velocity (initial velocity) at this moment. In the process of continuous outward dispersion, due to the different sizes and shapes of fragments and cabin debris, especially the natural fragments of cabin debris, their shapes were very different, so the aerodynamic drag coefficients of fragments and cabin debris were different. The fragments belonged to the general regular rectangle, and the aerodynamic drag coefficient was 1.24. The cabin debris belonged to the irregular rectangle, and the aerodynamic drag coefficient was 1.5. The aerodynamic force coefficient of fragments was smaller than that of cabin debris; that is, the attenuation coefficient of fragments was smaller than that of cabin debris. The fragments and cabin debris showed different attenuation laws in the process of dispersion.

4.3. Comparison with Experimental Value. The velocity-time history curve of fragments for warhead without cabin is shown in Figure 10(a). Also, the velocity-time history curve of fragments and cabin debris for warhead with cabin is shown in Figure 10(b) when $l/r = 0.2$.

From Figure 10, it can be seen that the fragment velocity of the noncabin warhead reached the maximum value of 1,766.9 m/s at about 50 μs after detonation loading, whose error is 4.8%, compared with the experimental value. When $l/r = 0.2$, the fragment velocity of the noncabin warhead reached the maximum value of 1,245.6 m/s at about 50 μs after detonation loading, whose error is −2.8%, compared with the experimental value. The fragment velocity of the cabin reached the maximum value of 1,892.8 m/s at about 80 μs, whose error is 3.2%, compared with the experimental value.

5. The Influence Law of Interval Distance

5.1. Action Sequence at Different Interval Distances. In order to analyze the dispersion process of fragments and cabins driven by detonation at different interval distances, numerical simulations were carried out under the conditions when $l/r = 0$, 0.1, 0.4, 0.6, 0.8, 1, and 2, respectively. The numerical simulation results of the detonation drive under three typical conditions when $l/r = 0$, 0.8, and 2 are given in Figures 11–13.

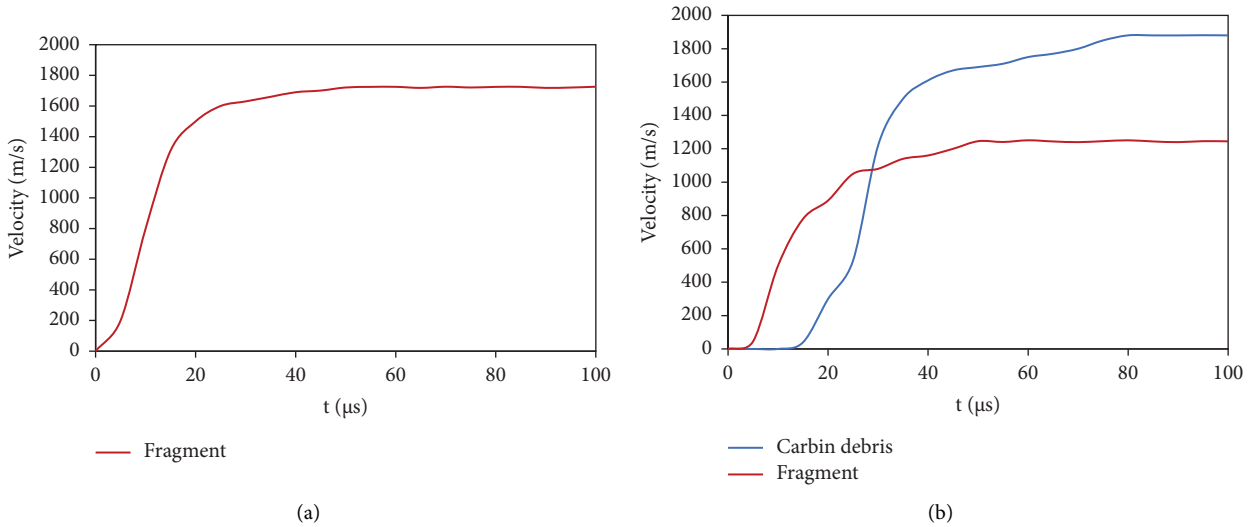

Figure 10: History curve of velocity to time. (a) Noncabin. (b) $l/r = 0.2$.

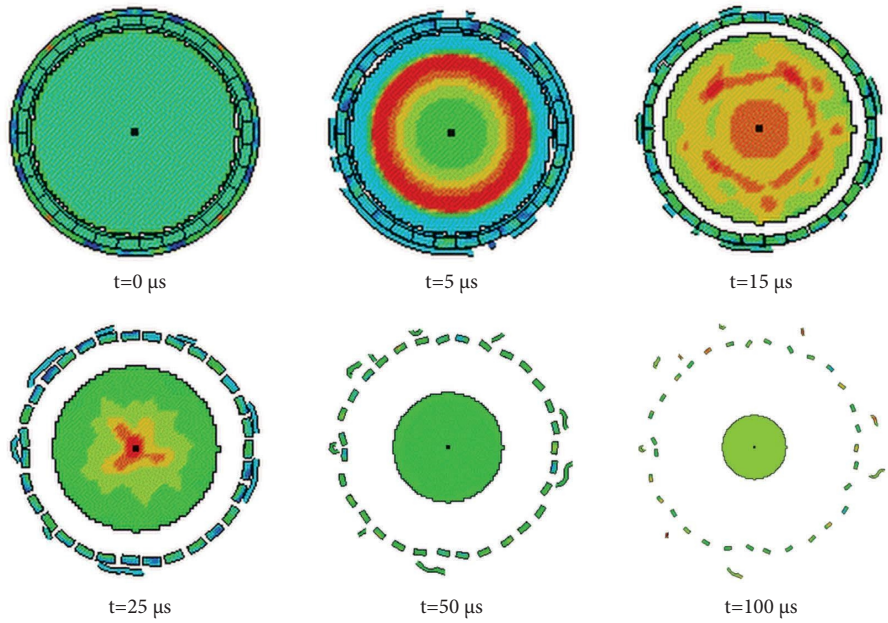

Figure 11: Denotation driving process of cabin-containing warhead when $l/r = 0$.

It can be seen from Figures 11 to 13 that when $l/r = 0$ and the detonation wave of the explosive propagated to the inner surface of the fragment, the fragment dispersed outward under the combined action of the detonation wave and the detonation gas product. Also, the detonation product overflowed from the fragment gap. Because there was no gap between the cabin and the fragment, the fragment collided with the cabin at the moment of outward dispersion. Under the combined action of the detonation gas product and the fragment, the cabin was broken immediately, that is, the three stages (II), (III), and (IV) occurred simultaneously. When $l/r = 0.8$, due to the large interval distance, the cabin began to expand and the rupture time was obviously delayed. When the fragment reached the initial velocity, the cabin was not completely ruptured, that is, the (V) stage was completed earlier than the (III) and (IV) stages. When $l/r = 2$, the interval distance reached 2 times the charge radius. It can be seen that at the time of 50 μs, the cabin had not begun to expand when the fragment reached the initial velocity, that is, the fragment was not affected by the cabin at the initial stage of growth under explosive detonation loading. After that, the fragment further dispersed outward and collided with the cabin.

Table 5 shows the action sequence of fragments and cabins under detonation loading at different values of l/r.

It can be seen from Table 5 that the time t_1 when the detonation product began to overflow at different interval distances was the same, all of which were 5 μs. The time t_2 when

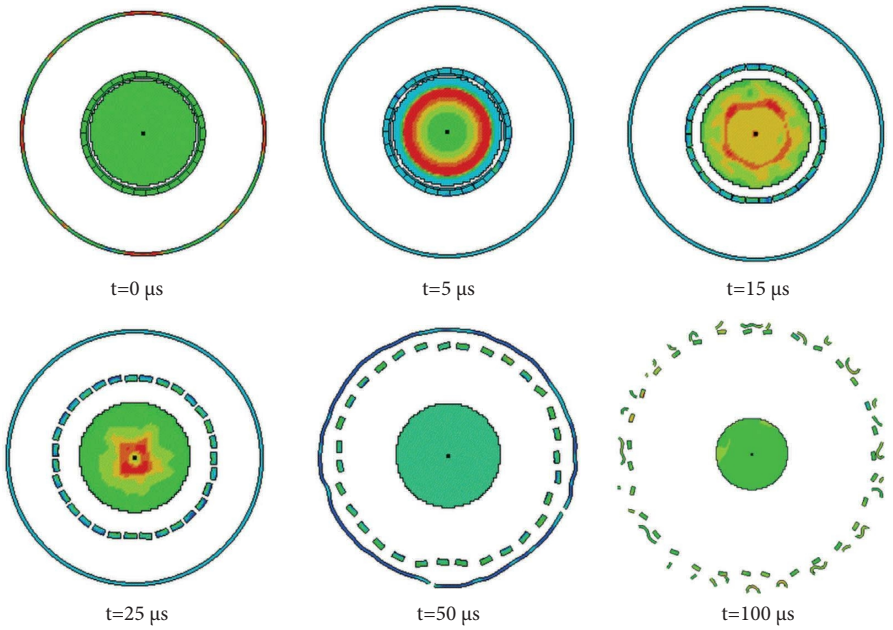

Figure 12: Denotation driving process of cabin-containing warhead when $l/r = 0.8$.

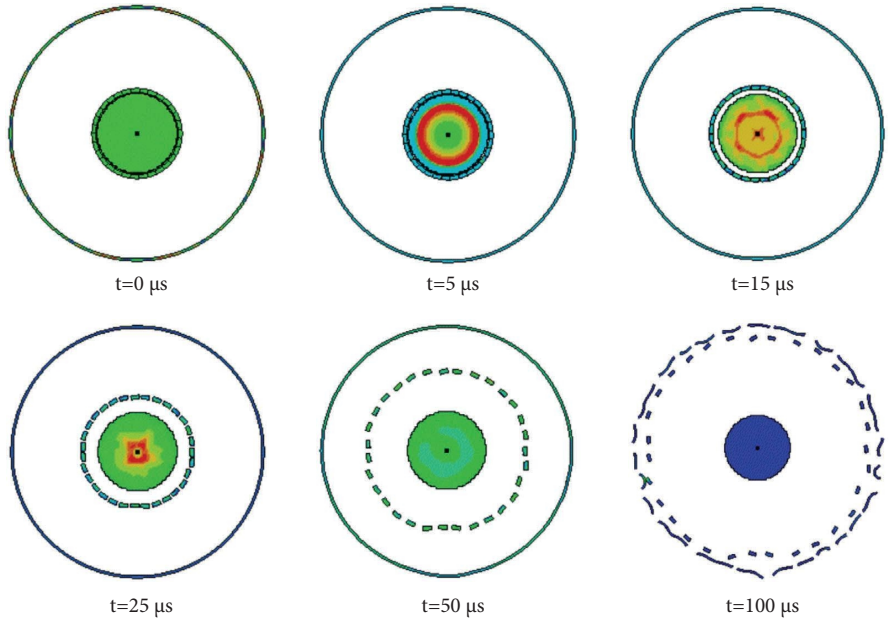

Figure 13: Denotation driving process of cabin-containing warhead when $l/r = 2$.

Table 5: Action sequence of fragments and cabins under detonation loading at different values of l/r.

l/r	Time (μs)												
	t_1	t_2	t_3	t_4	t_5	t_6	t_7	t_8	$t_2 - t_1$	$t_5 - t_2$	$t_6 - t_4$	$t_7 - t_6$	$t_8 - t_6$
0	5	5	5	5	16	14	50	80	0	11	9	22	66
0.1	5	13.4	16.8	22.6	28.2	29.2	50	80	8.4	14.8	6.6	20.8	50.8
0.2	5	18.2	20.4	25	35	30	50	80	13.2	16.8	5	20	50
0.4	5	20.4	28.4	34.2	42.2	39	50	80	15.4	21.8	4.8	11	41
0.6	5	24.6	34.8	39.4	48.4	42.6	50	80	19.6	23.8	3.2	7.4	37.4
0.8	5	28.0	44.4	50.2	58.6	76.8	50	80	23	30.6	26.6	—	3.2
1	5	32	49	59	64	81	50	90	27	32	22	—	9
2	5	55	73	105	112	126	50	140	50	57	21	—	14

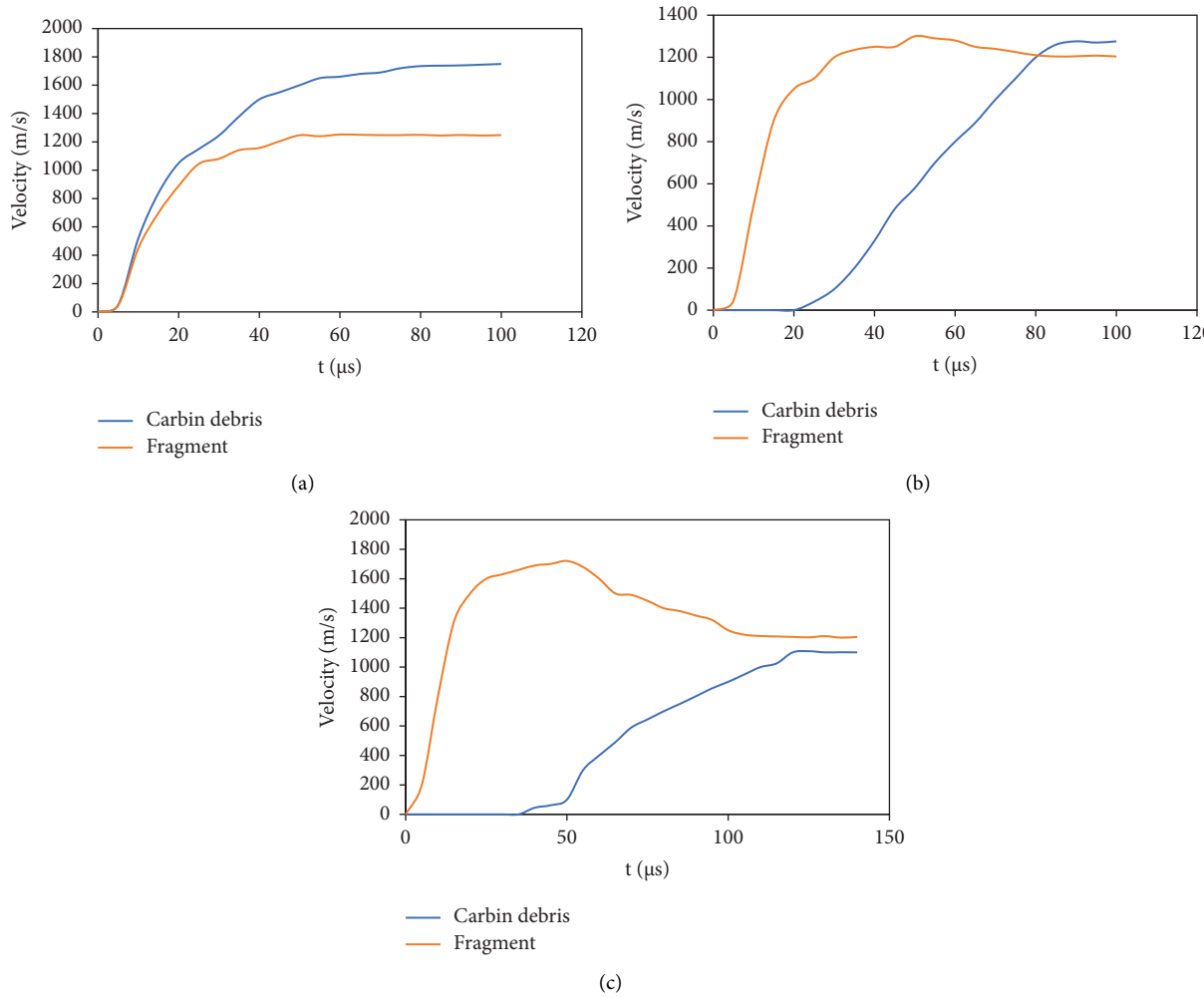

Figure 14: Velocity-time curves. (a) $l/r = 0$. (b) $l/r = 0.8$. (c) $l/r = 2$.

the cabin began to expand, the time t_3 when the cabin began to rupture, and the time t_5 when the rupture ended increased with the increase of the interval distance. The collision time t_4 and the separation time t_6 of the fragments and the cabin debris increased with the increase of the interval distance. The time t_7 at which the fragments reached the initial velocity was the same at different interval distances, all of which were 50 μs. When $l/r \leq 0.8$, the time t_8 when the cabin debris reached the initial velocity was 80 μs and then increased with the increase of the interval distance. At the same time, it can be seen that the sequence of t_5 at the end of the rupture of the cabin and t_6 at the time of separation of the fragments from the cabin debris was related to the interval distance. When $l/r < 0.8$, $t_5 > t_6$; when $l/r > 0.8$, $t_6 > t_7$. The sequence of t_6 at the time of separation of the fragments from the cabin debris and t_7 at the time when the fragments reached the initial velocity was related to the interval distance. When $l/r \leq 0.8$, $t_6 < t_7$. When $l/r > 0.8$, $t_6 > t_7$. It indicates that the interval distance has an important influence on the time sequence of the fragments and the cabin debris.

When $l/r \leq 2$, the detonation product overflow time $(t_2 - t_1)$ and the expansion rupture time $(t_5 - t_2)$ of the cabin increased with the increase of the interval distance. When $l/r < 0.8$, the collision separation time $(t_6 - t_4)$, the further acceleration time $(t_7 - t_6)$, and the further acceleration time $(t_8 - t_6)$ of the fragments decreased with the increase of the interval distance. When $l/r \geq 0.8$, the collision separation time between the fragments and the cabin debris increased significantly and decreased with the increase of the interval distance. When $l/r \geq 0.8$, the time for the fragments to reach the initial velocity was advanced. Therefore, there was no further acceleration phase, and the further acceleration time of the cabin debris increased with the increase of the interval distance. In summary, it can be seen that when $l/r = 0.8$, the action sequence of fragments and cabin debris shows significant characteristics.

5.2. The Relation between Velocity and l/r. Figure 14 shows the numerical simulation results of the velocity-time history curves of fragments and cabin debris under three typical working conditions when $l/r = 0$, 0.8, and 2.

It can be seen from Figure 14 that when $l/r = 0$, the cabin debris velocity was significantly greater than that of the fragment, in which the cabin debris velocity was 1, 750.6 m/s and the fragment velocity was 1, 252.7 m/s. The simulation results are basically the same as the simulation results when

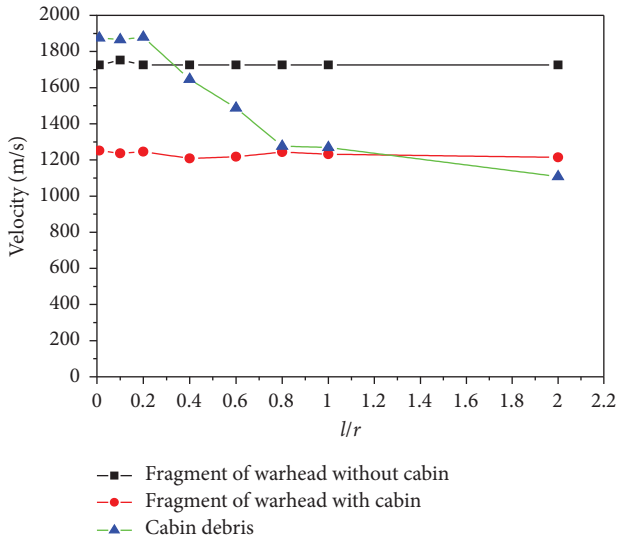

Figure 15: Relationship among fragment velocity, cabin debris velocity, and l/r.

$l/r = 0.2$. The difference is that when the spacing distance was 0, the fragment and the cabin debris accelerated at the same time, and there was no intersection collision point between the fragment and the cabin debris. When $l/r = 0.8$, the cabin debris velocity was still greater than that of the fragment, but the difference between the two was obviously reduced. The cabin debris velocity was 1, 301.1 m/s, and the velocity of the fragment was 1, 244.6 m/s. When $l/r = 2$, the fragment velocity was greater than the cabin debris velocity, and the fragment velocity showed a trend of increasing first and then decreasing. The maximum fragment velocity was basically the same as that without the cabin, reaching 1,720.8 m/s. It shows that when the interval distance increased to a certain value, the fragment acceleration process was not affected by the cabin, but the fragment velocity was reduced to 1,214.7 m/s due to the blocking of the cabin during the later scattering process.

Figure 15 shows the relationship among fragment velocity, cabin debris velocity, and l/r.

It can be seen from Figure 15 that the fragment velocity of the warhead with cabin was basically the same at different interval distances, and it was smaller than that of the warhead without cabin. It indicates that the interval distance has the same influence on the fragment velocity. When $l/r < 0.8$, the velocity of the cabin debris was greater than fragment of the warhead with cabin, and even greater than fragment of the warhead without cabin. When $l/r = 0.8$, the velocity of the cabin debris was approximately the same as fragment of the warhead with cabin. When $l/r = 2$, the velocity of the cabin debris is smaller than fragment of the warhead with cabin.

However, it should be pointed out that the maximum value of l/r was set to 2 in the above research. It is easy to imagine that when l/r is equal to infinity, the fragment velocity will no longer be affected by the cabin. That is to say, when l/r further increases on the basis of 2, there exists a critical interval distance, at which point the fragment velocity is no longer affected by the cabin. Considering the actual distance between the missile cabin and the warhead is generally relatively small and does not exceed the scope of this study, no research has been conducted on fragment velocity at larger intervals.

6. Conclusions

In this paper, the theoretical equation of fragment velocity of the warhead with cabin was established. Based on this, it can be inferred that part of the energy of the explosive in the warhead is used to drive the cabin debris so that the fragment velocity is reduced. Then, the fragment velocity and the cabin debris velocity of the cabin-containing warhead were studied by the static explosion experiments of a typical prototype, the results indicate that the experimental results of fragment velocity are consistent with the theoretical derivation results, and the velocity of cabin debris is greater than that of fragment of warheads without any cabin. Also, the detonation driving process of the warhead with cabin was described, which can be roughly divided into six stages: (I) fragment driving acceleration stage; (II) overflow stage of detonation products; (III) expansion and rupture stage of the cabin; (IV) collision and separation stage of fragments and cabin debris; (V) further acceleration stage of fragments and cabin debris; (VI) stable flying phase of fragments and cabin debris. Most importantly, this article confirms that the interval distance has a significant impact on the velocity of fragments and the velocity of cabin debris. When the ratio of the interval distance to charge radius (l/r) is no more than 2, the fragment velocity is basically the same, and the interval distance has the same effect on the fragment velocity. However, the velocity of the cabin debris decreases with the increase of the interval distance. When $l/r = 0.8$, the velocity of the cabin debris is approximately equal to the velocity of the fragment. When $l/r = 2$, the cabin debris velocity is less than the fragment velocity. When designing the structure and evaluating the power of a warhead with a cabin, the influence of the cabin on the velocity of fragments cannot be ignored, and cabin fragments are also an important element in destroying targets.

Data Availability

The data used to support the findings of this study are included within the article.

Conflicts of Interest

The authors declare that they have no conflicts of interest.

References

[1] R. W. Gurney, "The initial velocities of fragments from bombs, shells and grenades," Report No 405, Ballistic Research Laboratories (BRL), Aberdeen Proving Ground, MD, USA, 1943.

[2] T. Hiroe, K. Fujiwara, H. Hata, and H. Takahashi, "Deformation and fragmentation behaviour of exploded metal cylinders and the effects of wall materials, configuration,

explosive energy and initiated locations," *International Journal of Impact Engineering*, vol. 35, no. 12, pp. 1578–1586, 2008.

[3] D. Felix, I. Colwill, and E. Stipidis, "Real-time calculation of fragment velocity for cylindrical warheads," *Defence Technology*, vol. 15, no. 3, pp. 264–271, 2019.

[4] D. F. Zhu, C. G. Feng, Y. Li, and B. Li, "Calculation of first velocity of the unsymmetrical warhead fragment based on Gurney hypothesis," *Journal of Projectiles, Rockets, Missiles and Guidance*, vol. 26, no. 1, pp. 74–76, 2006.

[5] H. Grisaro and A. N. Dancygier, "Numerical study of velocity distribution of fragments caused by explosion of a cylindrical cased charge," *International Journal of Impact Engineering*, vol. 86, pp. 1–12, 2015.

[6] Y. G. Gao, S. S. Feng, X. Xiao, Y. Feng, and Q. Huang, "Fragment characteristics from a cylindrical casing constrained at one end," *International Journal of Mechanical Sciences*, vol. 248, Article ID 108186, 2023.

[7] L. J. Zhang and F. Shen, "Research on the initial velocity gradient of explosively driving double-layered spherical fragments," *Science Technology and Engineering*, vol. 15, no. 25, pp. 135–138, 2015.

[8] Y. Ma, Y. He, C. T. Wang, Y. He, and L. Guo, "Response behavior of double layer tungsten fragments under detonation loading," *Journal of Northwestern Polytechnical University*, vol. 40, no. 4, pp. 819–828, 2022.

[9] Y. J. Song, T. Zhou, F. Shen, and H. Wang, "Research on the behavior of initial stage about explosively-driven double-layered premade fragments," *Chinese Journal of Explosives and Propellants*, vol. 41, no. 3, pp. 308–313, 2018.

[10] L. K. Yin and J. W. Jiang, "Calculation model of initial velocity field on multilayered spherical fragments warhead," *Energetic Materials*, vol. 22, no. 3, pp. 300–305, 2014.

[11] D. Y. Shi, Q. M. Zhang, and C. F. Xia, "Numerical simulation method and different initiation modes for prefabricated multilayer fragment warhead," *Journal of PLA University of Science and Technology (Natural Science Edition)*, vol. 10, no. 6, pp. 553–558, 2009.

[12] Z. C. Wang, C. L. Jiang, and Z. Y. Chang, "Numerical study on double layers fragment warhead under asymmetrical initiation," *Advanced Materials Research*, vol. 424-425, pp. 471–475, 2012.

[13] P. J. Konig, "A correction for ejection angles of fragments from cylindrical wareheads," *Propellants, Explosives, Pyrotechnics*, vol. 12, no. 5, pp. 154–157, 1987.

[14] L. Wang, F. Han, and Q. Zhou, "The projection angles of fragments from a cylindrical casing filled with charge initiated at one end," *International Journal of Impact Engineering*, vol. 103, pp. 138–148, 2017.

[15] X. Li, W. L. Wang, and Z. F. Liang, "Dispersion characteristics of fragments of the warhead under different initiation modes," *Journal of Projectiles, Rockets, Missiles and Guidance*, vol. 42, no. 4, pp. 35–42, 2022.

[16] J. Xia, *Missile*, Chemical Industry Press, Beijing, China, 2009.

[17] Z. J. Wang and J. P. Yin, *Ammunition*, Beijing University of Technology Press, Beijing, China, 2005.

[18] L. W. Liu, "Design and evaluation of composite material guidance cabin for improved sea sparrow missile," *Winged Missiles Journal*, vol. 52, no. 1, pp. 58–62, 2003.

[19] D. V. Kien, D. N. Anh, and D. N. Thai, "Numerical simulation of the stability of rock mass around large underground cavern," *Civil Engineering Journal*, vol. 8, no. 1, pp. 81–91, 2022.

[20] Y. Tahir, I. Kadiri, S. E. Fertahi et al., "Design of controlled pre-split blasting in a hydroelectric construction project," *Civil Engineering Journal*, vol. 9, no. 3, pp. 556–566, 2023.

[21] R. Balamuralikrishnan, A. S. H. Al-Mawaali, M. Y. Y. Al-Yaarubi, B. B. Al-Mukhaini, and A. Kaleem, "Seismic upgradation of RC beams strengthened with externally bonded spent catalyst based ferrocement laminates," *High Tech and Innovation Journal*, vol. 4, no. 1, pp. 189–209, 2023.

[22] T. Bangia and R. Raskar, "Cohesive methodology in construction of enclosure for 3.6 m devasthal optical telescope," *High Tech and Innovation Journal*, vol. 3, no. 2, pp. 162–174, 2022.

[23] Y. B. Sun, *Explosive Action and Charge Design*, National Defense Industry Press, Beijing, China, 1987.

[24] L. P. Orlenko and C. W. Sun, *Explosive Physics*, Science Press, Beijing, China, 2011.

[25] J. Szmelter, N. Davies, and C. K. Lee, "Simulation and measurement of fragment velocity in exploding shells," *Journal of Battlefield Technology*, vol. 10, no. 2, pp. 1–7, 2007.

[26] N. M. Hu, X. Zhu, and C. H. Chen, "Theoretical calculation of the fragment initial velocity following aerial explosion of the cylindrical warhead with two terminals," in *Proceedings of the IOP Conference Series: Materials Science and Engineering*, vol. 274, p. 012049, Changsha, China, October 2017.

[27] B. Y. Hu, Q. D. Dong, C. S. Han, and M. Zhang, "Analysis of the firing mechanics for Ti-6Al-4v natural fragments," *Explosion and Shock Waves*, vol. 15, no. 3, pp. 254–258, 1995.

[28] Z. K. Meng, C. W. Tan, and S. Y. Sui, "Study about the phase structure of titanium alloy material used in semi-armor piercing warhead," *Journal of Astronautics*, vol. 28, no. 5, pp. 1362–1365, 2007.

[29] H. Deng, J. L. Quan, and Z. F. Liang, "Influence of eccentric initiation on energy distribution gain of a warhead charge," *Explosion and Shock Waves*, vol. 42, no. 5, 2022.

[30] C. Z. Miao, Z. Y. Liang, D. Z. Deng, F. D. Liang, and M. G. Wang, "Numerical simulation influence of curvature radius on focusing warhead," *Ordnance Industry Automation*, vol. 37, no. 12, pp. 93–96, 2018.